Design and Calibration of a Piezoelectric Force Sensor for Bearing Fault Detection

Ali Safian[1], Nan Wu[1], Xihui Liang[1*]
[1]Department of Mechanical Engineering, University of Manitoba, Winnipeg, Canada
*Xihui.Liang@umanitoba.ca

Abstract— With the advent of IoT and trends toward intelligent manufacturing, having mechanical systems with integrated sensors is becoming more popular. Bearings are one of the components that have attracted more attention toward being integrated with sensors. Therefore, in this research, the design and modeling of a low-cost piezoelectric force sensor embedded inside the bearing housing have been investigated. Through using a reference force sensor, the designed piezoelectric force sensor is calibrated. Also, a theoretical model is developed to estimate the sensitivity of the sensor for low and high frequencies. By performing a modal analysis and harmonic test, the frequency response of the sensor up to the first natural frequency is obtained. Subsequently, the proposed sensor is integrated with a previously developed bearing dynamic model to analyze the sensor response in case of having a local fault on the outer ring. According to the results, the proposed sensor is capable of detecting local fault symptoms on the bearing outer ring in the frequency domain.

Keywords-Smart bearing; bearing fault; finite element model; piezoelectric; force sensor

I. INTRODUCTION

Rolling element bearings are one of the most important components in the majority of rotating machines. These components control the rotation and load of the shaft with low friction to prevent excessive wear during the operation of the system. The existence of a minor defect in bearing, whether made by manufacturing error or occurred during the operation, can be gradually extended to severe wear, spalling, and cracks. These situations finally can lead to breakdown and abrupt failure in the machine. For many years, vibration condition monitoring has been an effective method in detecting faults in rotating machines. Typically, an accelerometer sensor is mounted on the bearing housing and the trend of vibration is captured over a period of time. If there is an excessive vibration more than the threshold, the system is flagged or in severe cases, it is stopped for replacing the faulty bearing [1]. However, there are a few drawbacks to using accelerometers for bearing fault detection. For example, accelerometers are sensitive to surrounding noise and vibration. This drawback creates practical difficulties in noisy industrial settings where several machines are working simultaneously. In addition, the majority of accelerometers are installed on the machine or the bearing housing, which means there is a long transmission path between the sensor and the defect. Subsequently, early fault symptoms lose their energy to reach the sensor and might be masked by surrounding noise and structural resonances [2].

To overcome the aforementioned problems, various research papers have been published about using embedded sensors in the bearing housing to create a shorter transmission path. In this way, the early fault symptoms require a shorter path to reach the sensor, and the signal-to-noise ratio (SNR) will be increased. For example, Alian et al. [3] implemented embedded fiber Bragg grating sensors (FBG) to measure local strain changes in the close vicinity of the bearing. According to the results, the SNR was enhanced compared with an accelerometer sensor and it was reported that measurement of local strain changes is less susceptible to the surrounding noise. However, FBG sensors are expensive and have a low-frequency bandwidth which makes them an inappropriate choice for high-speed cases. In addition to FBG sensors, several researchers proposed using embedded piezoelectric materials for bearing condition monitoring. These materials work under the principle of piezoelectricity and convert a mechanical input into a proportional electric charge. Piezoelectric sensors have a high frequency bandwidth due to their solid structure, do not require bulky measurement devices, and are comparatively cheap [4]. As a few examples, Nicholas et al. [5] implemented piezoelectric sensors to measure roller load and lubrication by ultrasonic reflectometry technique. Russel et al. [6] mounted a thin film of a piezoresistive force sensor in between the housing and outer ring for evaluating load distribution. Except for bearing applications, piezoelectric force sensors are also designed for other applications such as milling force measurement [7] and pressure sensors [8].

According to the literature, there is no comprehensive research about designing and using piezoelectric ceramics in bearings for fault detection and force monitoring. A common type of these ceramics is Lead Zirconate Titanate, known as PZT materials, which are available in various sizes and shapes [4]. In

contrast with polymer-based piezoelectric films, PZT materials have higher rigidity and natural frequency with a lower price, making them a good choice for sensing applications. In this research, PZT materials are utilized for designing a force sensor inside a bearing housing. In addition, a general procedure is explained, which can be used for designing and calibrating any force, strain, and pressure sensors made by PZT materials. After the design and calibration part, the response of the designed sensor is investigated employing a dynamic finite element method (FEM), where a cylindrical roller bearing with an integrated PZT material is created in ANSYS APDL. The response of the sensor in healthy and defective conditions is presented to investigate the fault detection abilities of this sensor.

II. MEASURING PRINCIPLE OF PIEZOELECTRIC SENSORS

In this section, the measuring principle and theoretical formulation of piezoelectric materials are explained. This procedure is a general approach and can be used for sensing and energy harvesting applications. Generally, the electromechanical behaviour of piezoelectric materials is defined by piezoelectric constitutive equations. Depending on the target output of the theoretical modeling, different forms of these equations can be used, such as stress-charge mode or strain-charge mode. For a piezoelectric disk under radial loading, as shown in Figure 1, the constitutive equation in strain-charge mode is as follows [9]:

$$\begin{cases} S_p = s_{pq}^E T_q + d_{ip} E_i \\ D_i = d_{iq} T_q + \varepsilon_{ik}^T E_k \end{cases} \qquad (1)$$

where, S_p refers to strain; T_q, stress; D_i, electric displacement; d_{iq}, piezoelectric matrix; E_i, electric field; and ε_{ik}^T, permittivity matrix in constant stress. Here, the subscript i and k refer to numbers from 1 to 3, and p and q indicate the numbers from 1 to 6. It is worth mentioning that numbers 1 to 3 represent the directions in the coordinate system as shown in Figure 1, and numbers 4 to 6 are related to the shear directions. For an open circuit condition under radial loading, the electric displacement is zero ($D_3 = 0$). Considering that electric field (E_3) can be written as $E_3 = V/h$, where V and h represent voltage and piezoelectric height, respectively, the Eq (1) can be rewritten as [9]:

$$D_i = 0 = d_{33} \frac{F}{A} + \varepsilon_{33}^T \frac{V}{h} \qquad (2)$$

$$V = -\frac{h d_{33} F}{\varepsilon_{33}^T A} \qquad (3)$$

where F and A stand for radial force and piezoelectric area, respectively. The generated voltage from Eq (3) is in an open
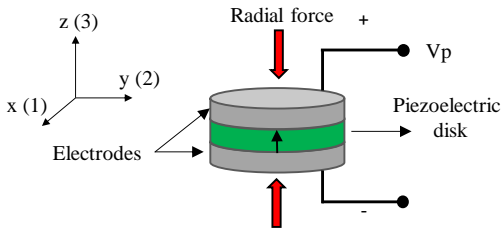

Figure 1. Example of a piezoelectric disk under radial loading.

circuit condition which is an ideal situation where there is no electric charge dissipation. This means if the measurement device like a voltmeter has a significantly large resistance, the experimental voltage will match the open circuit condition and the voltage signal exactly follows the trend of applied force/strain. In this condition, the frequency of applying force/strain is not significantly influencing the output voltage. However, in reality, the measurement devices do not have high resistance, and the electric charge finds the path with the lowest resistance to discharge immediately. This condition can be modelled by using the constitutive equations and including the circuit resistance [10]. A general approach for the stress-charge mode of the piezoelectric material by considering the resistance is explained in reference [11]. However, in this research, a similar approach is adopted for strain-charge mode conditions for modeling and calibration of a piezoelectric force sensor. Therefore, Eq (1) can be rearranged as follows:

$$V - \frac{h D_3}{\varepsilon_{33}^T} = -\frac{d_{33} h T_3}{\varepsilon_{33}^T} \qquad (4)$$

Considering that $D_3 = Q/A$, where Q is the electric charge, the first derivative of D_3 equals -i/A, which i refers to the current. In addition, the capacitance of the piezoelectric can be defined by $C_p = \varepsilon_{33}^T A/h$. Hence, applying the first derivative to Eq (4) results in the following equation:

$$\dot{V} + \frac{1}{C_p R} V = -\frac{d_{33} h}{\varepsilon_{33}^T} \cdot \frac{dT_3}{dt} \qquad (5)$$

where R refers to the circuit resistance. According to the general solution of a first-order non-homogeneous linear differential equation, and relation of stress and force ($T_3 = F/A$), the solution to Eq (5) is obtained by:

$$V(t) = e^{-\frac{t}{C_p R}} \cdot \frac{-d_{33} h}{\varepsilon_{33}^T A} \int_0^t e^{\frac{t}{C_p R}} \cdot \frac{dF}{dt} \qquad (6)$$

By tuning the resistance in Eq (6), it can be observed that the voltage signal will significantly decrease by low resistance. Nevertheless, the voltage increases up to open-circuit voltage for large values of the resistance. This procedure will be used in the next section to estimate the circuit resistance after calibrating the force sensor.

III. DESIGN AND CALIBRATION OF PIEZOELECTRIC FORCE SENSOR

In this section, the details of the sensor modeling integrated with a bearing dynamic model are explained. In addition, the procedure for calibrating and estimating the circuit resistance is presented. By using the estimated circuit resistance, a FEM model is created to obtain the frequency response of the sensor under harmonic excitation and predict the frequency range of the sensor.

A. Simulation of a Bearing with an Integrated PZT Sensor

For simulating the applied force on the PZT sensor during the rotation of the bearing, a bearing dynamic model is adopted from references [2] and [12] with minor changes. The bearing type for this modeling is SKF N350 ECP with a split housing type
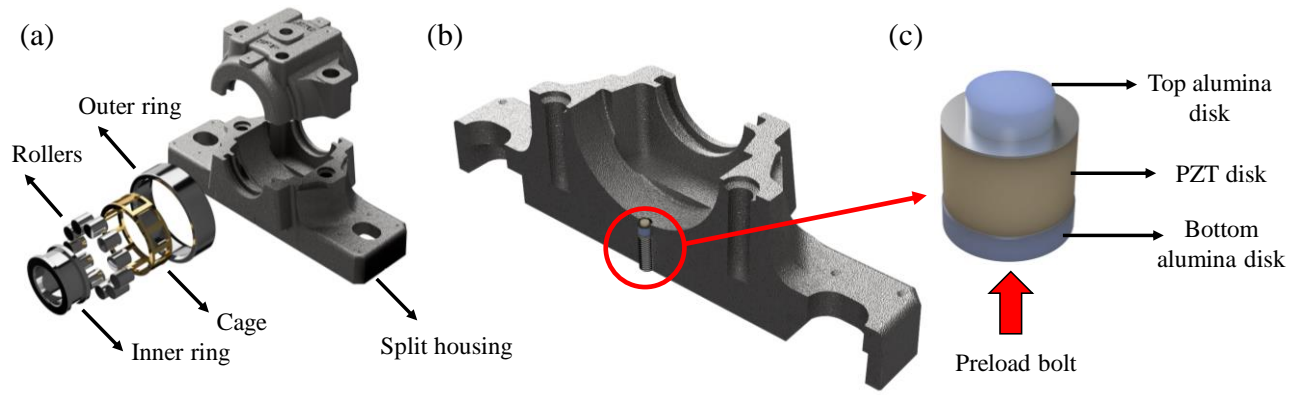
Figure 2. (a) Explosive view of the bearing components, (b) cross-section view of the split housing and sensor, and (c) sensor configuration.

SNL 506-605 as illustrated in Figure 2(a) and Figure 2(b). In the center of the housing, a threaded hole is created where a PZT sensor is mounted. The configuration of the sensor is illustrated in Figure 2(c), which includes a PZT disk with a diameter of 4.7 mm and a height of 3.4 mm covered by two layers of alumina disks. The alumina disks have 3 and 5 mm diameters with 1mm thickness and are made by nonporous alumina ceramics.

In order to simulate this bearing assembly with the PZT sensor, the bearing outer ring and the housing are modelled by ANSYS APDL as shown in Figure 3. Since this cylindrical roller bearing has a zero contact angle and is designed for radial loading, the strain changes in the axial direction are negligible. Therefore, by applying symmetric boundary condition ($Ux = 0$), only half of the bearing and the housing thickness is modelled as shown in Figure 3(a). According to references [2] and [12], the inner ring and the rollers are not modelled, and instead, roller contact forces are applied to small contact regions over time. These contact forces are obtained by means of a 4 degree-of-freedom lumped parameter model (LPM) developed in MATLAB. Depending on the region of interest, a fine mesh is applied to that region, and dynamic load from the LPM is only applied to those areas. This feature reduces the complexity and computational time of the FEM model by eliminating non-linearity due to rollers' contact and reducing the number of elements. For further modeling details, readers are encouraged to refer to references [2] and [12]. In Figure 3(b), the back view of

the bearing outer ring without the housing and the position of the PZT sensor in contact with the outer ring is illustrated. Since the alumina ceramic has high mechanical strength, the compressibility of the bottom alumina disk is negligible and instead, the radial displacement of the bottom surface of the PZT disk is constrained ($Uz = 0$). For simulating the local defect, a small portion of the outer ring is removed. The width and depth of the defect are 0.9 mm and 1 mm, respectively.

The material properties of the housing, outer ring, and alumina ceramics are presented in Table 1. For these three components, the element type of SOLID185 is considered in ANSYS. The PZT disk is made by APC 850 (Naby type II), and the material properties are presented in the form of matrices in Eq (7) to (9) [12]. The element type for the PZT material is SOLID266 which defines the electromechanical properties of the sensor. After applying the mesh and boundary conditions, the dynamic loads are applied to the bearing under 1000 rpm rotational speed. The solution time increment is equal to 0.392156×10^{-3} (s) which results in a sampling frequency around 2500 Hz. By running the transient analysis, the contact force between the PZT sensor and the outer ring is obtained over time in healthy and faulty situations. However, for modeling the voltage signal generated by the applied force, the resistance of the circuit needs to be estimated as mentioned in Eq (6). Through a calibration procedure, the resistance of the circuit is estimated.
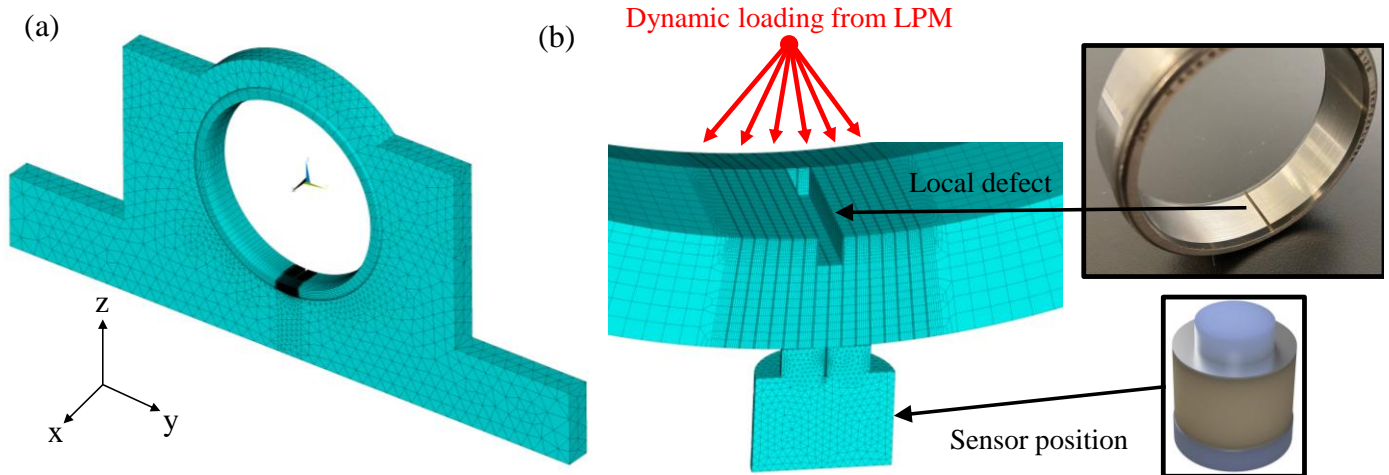

Figure 3. (a) Front view of the bearing FEM model and (b) back view of the model with zoomed view of local defect and sensor position.

TABLE I.   MATERIAL PROPERTIES IN THE FEM MODEL

Material (component)	Material property		
	Young's modulus (GPa)	*Poisson's ratio*	*Density (kg/m³)*
Cast Iron (housing)	110	0.28	7200
Steel (outer ring)	200	0.3	7800
Alumina ceramic (sensor protection disks)	330	0.22	3900

$$[\varepsilon^T]_{PZT} = \begin{bmatrix} 1800 & 0 & 0 \\ 0 & 1800 & 0 \\ 0 & 0 & 1800 \end{bmatrix} \times 8.85 \times 10^{-12} \frac{F}{m} \quad (7)$$

$$[d]_{PZT} = \begin{bmatrix} 0 & 0 & -175 \\ 0 & 0 & -175 \\ 0 & 0 & 400 \\ 0 & 590 & 0 \\ 590 & 0 & 0 \\ 0 & 0 & 0 \end{bmatrix} \frac{pC}{N} \quad (8)$$

$$[c]_{PZT} = \begin{bmatrix} 1.47 & 1.05 & 0.93 & 0 & 0 & 0 \\ 1.05 & 1.47 & 0.93 & 0 & 0 & 0 \\ 0.93 & 0.93 & 1.13 & 0 & 0 & 0 \\ 0 & 0 & 0 & 0.23 & 0 & 0 \\ 0 & 0 & 0 & 0 & 0.23 & 0 \\ 0 & 0 & 0 & 0 & 0 & 2.12 \end{bmatrix} \times 10^{11} \frac{N}{m^2} \quad (9)$$

B. Calibration of the PZT Force Sensor

In this section, the details of the sensor calibration are presented. As it was discussed in Section II, applying a mechanical load to a piezoelectric material result in a voltage value calculated by Eq (3). However, this equation is applicable if the measurement device has an infinite resistance which the voltage in the piezoelectric material equals open circuit condition [11]. This condition rarely happens, and the generated charge finds the path with the lowest resistance to discharge immediately. To estimate the circuit resistance and calibrate the PZT sensor accordingly, a reference force sensor can be utilized to measure the sensitivity of the PZT sensor in mV/N. Subsequently, the measured force signal by the reference sensor can be substituted into Eq (6) and by tuning the resistance (R), the circuit resistance can be estimated as well.

Figure 4 illustrates the reference force sensor and the raw PZT disk sample. The reference force sensor is the FlexiForce sensor manufactured by Tekscan, which includes a piezoresistive force sensor and an analog to digital converter that connects to a PC by a USB port. The sensing area of this sensor has a radius of 4.8 mm which is larger than the PZT disk. In addition, 2 m low-noise coaxial cable model PCB-003 is connected to the top and bottom electrodes by using copper tape. On the other end of the cable, a BNC connector transmits the generated voltage to a data acquisition system model Spider-80Xi. By applying a dynamic force using a foreign rod and hand force, two signals are collected simultaneously. One represents the applied dynamic load, and the other one gives the equivalent voltage signal.
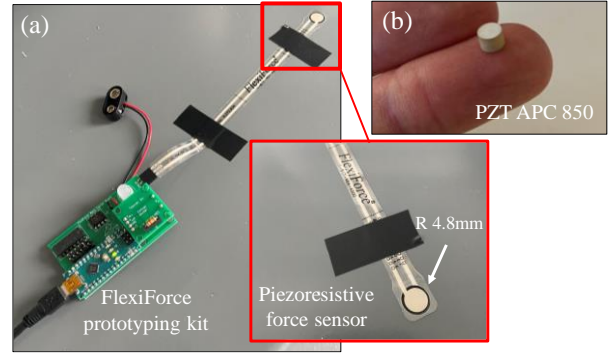

Figure 4.   (a) Reference force sensor setup with a piezoresistive sensor, and (b) the raw PZT APC 850.

Figure 5 shows the simultaneous voltage signal versus the applied dynamic force. During a 25 s period, 13 impulses are applied to the PZT disk, which results in a voltage and force signal with a frequency of about 0.5 Hz. By recording the peak value of each simultaneous signal, the division of voltage to force value gives the sensitivity of the PZT force sensor. Hence, averaging the calculated sensitivities from a few impulses gives the sensor sensitivity as 74.4 mV/N for the frequency of 0.5 Hz. However, the sensitivity of the piezoelectric materials is dependent on the frequency, and a frequency range needs to be reported, which has minor sensitivity changes. This process is discussed in the next section.
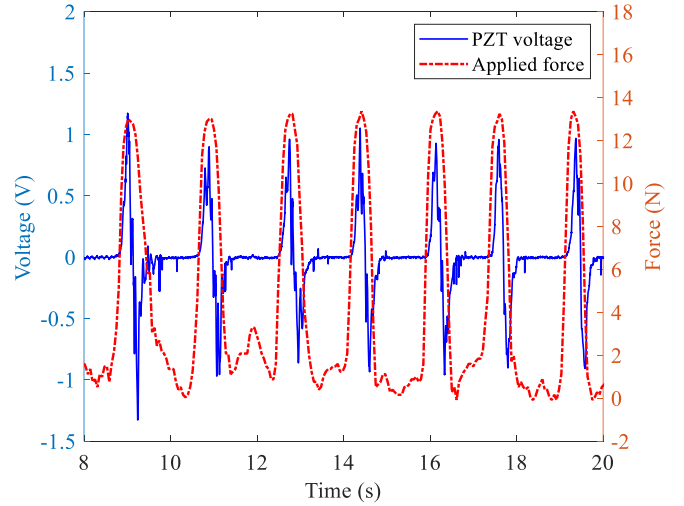

Figure 5.   Generated PZT voltage versus the applied dynamic load.

By calculating the sensitivity of 74.4 mV/N for the frequency of 0.5 Hz, the applied force in Figure 5 and the model parameters can be substituted in Eq (6). By entering a resistance value for the first try, such as 10 MΩ, the voltage signal can be simulated using the experimental force data. The resistance can be tuned by trial and error to match the voltage signal with the experimental voltage. Figure 6 presents the simulated voltage and experimental voltage signals after estimating a resistance of 50 MΩ. It is worth mentioning that for the coaxial cable model PCB-003, a capacitance of 90 pF/m is added to the PZT capacitance (C_p) according to the manufacturer datasheet. Comparing the simulated and experimental voltage in Figure 6 shows an appropriate correlation in the developed model. In the next section, the details of the frequency response are explained.
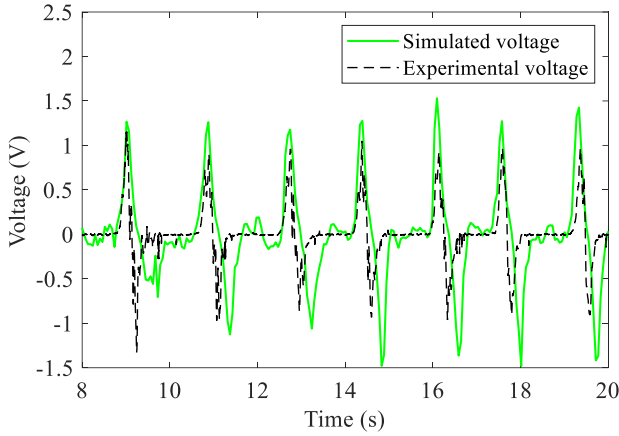
Figure 6. Comparison of the simulated and experimental voltage signals by the PZT force sensor.

C. Frequency Bandwidth Estimation

To investigate the sensitivity of the sensor in different frequencies, two different analyses have been conducted in this section. First, the sensitivity of the sensor in lower frequencies such as 1, 10, 20, and up to 100 Hz is calculated by using Eq (6). Through this part, the linearity of the sensor response in lower frequency and a reference sensitivity can be determined. In the second analysis, harmonic analysis is performed to estimate the frequency bandwidth of the sensor for high frequency applications.

Figure 7 presents the FEM model and the first mode shape of the sensor. Through a modal analysis, the first resonance frequency of the sensor is obtained to be 1.21×10^5 Hz. By using harmonic analysis and mode superposition method, a 1 N harmonic force is applied to the bottom of the sensor. Also, the top surface of the sensor is constrained to prevent rigid body motion. Through using element type CIRCU94, the resistance of the circuit, which was calculated in the previous section (50 MΩ), is applied to the model. This simulation gives the frequency response of the sensor up to 130 kHz.

Figure 8 illustrates the sensor sensitivity in low frequencies and the frequency response of the sensor for a wider frequency range. According to Figure 8(a), the linearity of the sensor sensitivity begins at the frequency of 30 Hz with a sensitivity deviation percentage below 5%. Therefore, the sensitivity at 30 Hz can be selected as the reference sensitivity which is equal to 0.36 V/N. Subsequently, the harmonic analysis gives the
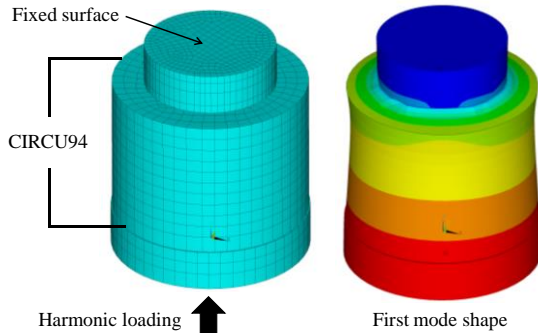

Figure 7. Sensor FEM model for harmonic analysis in ANSYS APDL.

frequency response for high frequencies up to the first natural frequency which is presented in Figure 8(b). For a +3dB deviation, which is about 27%, the frequency range of the sensor will be 30 Hz to 45 kHz.
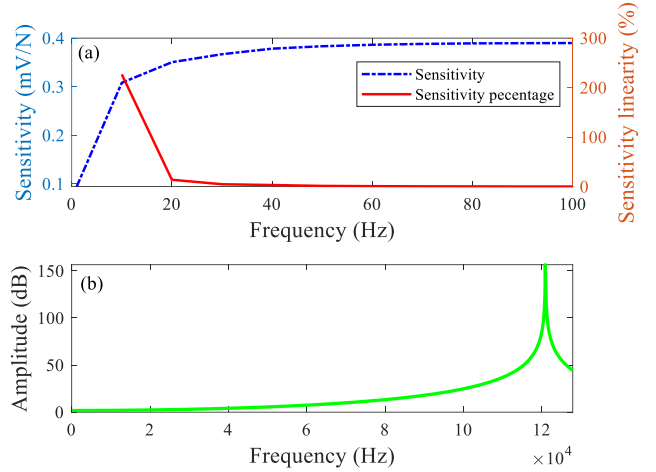

Figure 8. (a) Sensitivity deviation of the PZT sensor in low frequencies, and (b) high-frequency response of the sensor up to the first resonance.

IV. RESULTS AND DISCUSSION

So far, the sensitivity and frequency response of the sensor have been determined in the previous sections. In this section, the application of the sensor for bearing fault detection is investigated through the FEM model that was explained in section III. To compare the sensor performance in healthy and faulty conditions, the bearing model is simulated once without a local fault and once with a local fault as shown in Figure 3(b). During the rotation of the rollers, the strain changes in the thickness of the outer ring cause a reaction force between the sensor and the outer ring surface. Obviously, for higher radial loads from the shaft, the reaction force, and the generated voltage increase. For this simulation, a radial load of 500 N and a rotational speed of 1000 rpm (16.6 Hz) are considered. For the bearing type SKF N305 ECP which has 11 rollers, the rotational speed of 1000 rpm causes a ball pass frequency of 70.8 Hz on the outer ring of the bearing (BPFO) [2].

Figure 9 presents the voltage signal in the PZT sensor in healthy and faulty conditions. In both cases, the voltage amplitude is modulated by the passing rollers. This voltage signal can be
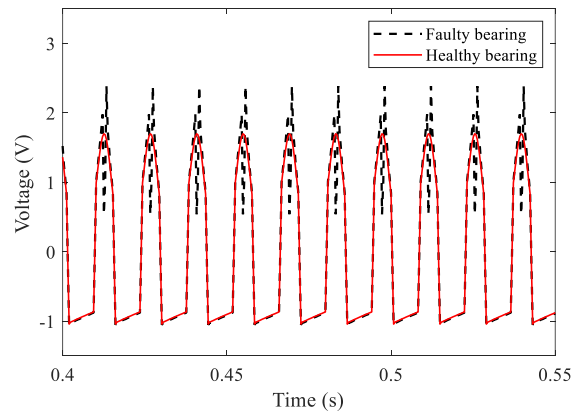

Figure 9. Simulated voltage signal by PZT sensor inside the bearing housing in healthy and faulty conditions.
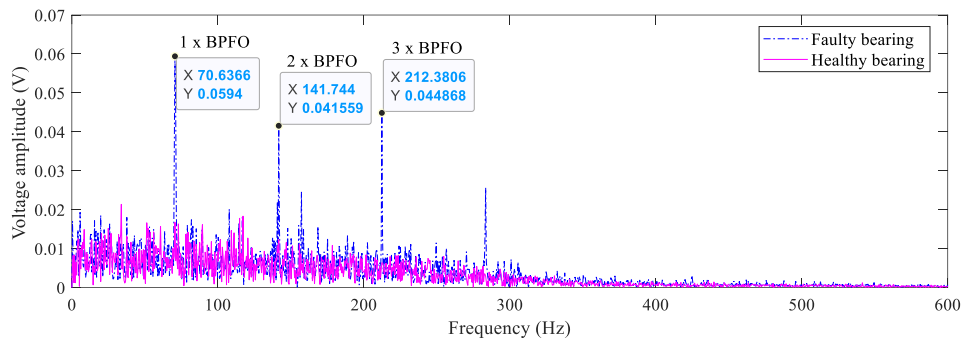
Figure 10. Envelope spectrum of the voltage signal by PZT sensor in healthy and faulty conditions.

converted to a force signal if the data points are divided by the sensor sensitivity. The major difference between these two cases is the sharp voltage impulses that are caused by contact force fluctuations in the faulty bearing. Converting this time domain voltage signal to frequency domain creates high amplitudes for BPFO and its harmonics which indicates the existence of a local fault on the outer ring. However, this time-domain signal is in an ideal condition in which there is not any noise from the measurement devices, triboelectric effect, and electromagnetic field. Therefore, to investigate the possibility of detecting fault symptoms, it is preferred to add some noise to the time domain signal prior to converting to the frequency domain.

Figure 10 demonstrates the envelope spectrum of the voltage signal in healthy and faulty conditions. By adding a white Gaussian noise with an SNR of 10, the fault detection ability of the sensor can be investigated in a noisy setting. According to this figure, the existence of local fault has significantly affected the BPFO and its harmonics. Therefore, it can be concluded that the proposed sensor has a good performance in detecting local fault symptoms.

As the future work of this study, the proposed sensor will be tested in an experimental test in a bearing test apparatus. Also, the effect of damage level and location will be investigated. More importantly, the performance of the proposed sensor compared with conventional accelerometers will be investigated at various rotational speeds.

CONCLUSION

In this research, the design and modeling of a piezoelectric force sensor for the application of bearing fault detection are investigated. A general theoretical approach is developed to simulate the voltage signal of a piezoelectric disk compared with an experimental test. By using a reference force sensor, the PZT sensor is calibrated and the sensitivity for low and high frequencies is investigated. Besides, a harmonic test is conducted to estimate sensitivity deviations in high frequencies. According to the results, the sensitivity of 0.36 V/m is obtained for the sensor that deviates up to 27% between the frequency range of 30 Hz to 45 kHz. By utilizing the estimated sensitivity and model parameters, the sensor is integrated with a previously developed bearing dynamic FEM model to investigate the fault detection abilities of the sensor. According to time and frequency domain analyses, the proposed sensor has an

appropriate performance in local fault detection on the outer ring of the bearing. Hence, the proposed sensor can be a potential sensor for developing smart bearings with integrated sensors.

REFERENCES

[1]   A. Moazen Ahmadi, C. Q. Howard, and D. Petersen, "The path of rolling elements in defective bearings: Observations, analysis and methods to estimate spall size," *J. Sound Vib.*, vol. 366, pp. 277–292, Mar. 2016, doi: 10.1016/j.jsv.2015.12.011.

[2]   A. Safian, H. Zhang, X. Liang, and N. Wu, "Dynamic simulation of a cylindrical roller bearing with a local defect by combining finite element and lumped parameter models," *Meas. Sci. Technol.*, vol. 32, no. 12, pp. 1–26, Dec. 2021, doi: 10.1088/1361-6501/ac2317.

[3]   H. Alian, S. Konforty, U. Ben-Simon, R. Klein, M. Tur, and J. Bortman, "Bearing fault detection and fault size estimation using fiber-optic sensors," *Mech. Syst. Signal Process.*, vol. 120, pp. 392–407, Apr. 2019, doi: 10.1016/j.ymssp.2018.10.035.

[4]   J. Sirohi and I. Chopra, "Fundamental Understanding of Piezoelectric Strain Sensors," *J. Intell. Mater. Syst. Struct.*, vol. 11, no. 4, pp. 246–257, Apr. 2000, doi: 10.1106/8BFB-GC8P-XQ47-YCQ0.

[5]   G. Nicholas, T. Howard, H. Long, J. Wheals, and R. S. Dwyer-Joyce, "Measurement of roller load, load variation, and lubrication in a wind turbine gearbox high speed shaft bearing in the field," *Tribol. Int.*, vol. 148, pp. 1–14, Aug. 2020, doi: 10.1016/j.triboint.2020.106322.

[6]   T. Russell, A. Shafiee, B. Conley, and F. Sadeghi, "Evaluating load distribution at the bearing-housing interface using thin film pressure sensors," *Tribol. Int.*, vol. 165, pp. 1–9, Jan. 2022, doi: 10.1016/j.triboint.2021.107293.

[7]   M. Luo, H. Luo, D. Axinte, D. Liu, J. Mei, and Z. Liao, "A wireless instrumented milling cutter system with embedded PVDF sensors," *Mech. Syst. Signal Process.*, vol. 110, pp. 556–568, Sep. 2018, doi: 10.1016/j.ymssp.2018.03.040.

[8]   Y. Li, Z. Yang, G. Wang, and C. Yang, "Research on piezoelectric pressure sensor for shock wave load measurement," *ISA Trans.*, vol. 104, pp. 382–392, Sep. 2020, doi: 10.1016/j.isatra.2020.05.018.

[9]   A. L. Gama, W. B. de Lima, J. A. Santisteban, and João. P. S. de Veneza, "Proposal of New Strain Transducers Based on Piezoelectric Sensors," *IEEE Sens. J.*, vol. 15, no. 11, pp. 6263–6270, Nov. 2015, doi: 10.1109/JSEN.2015.2454858.

[10] Q. Li, S. Li, D. Pisignano, L. Persano, Y. Yang, and Y. Su, "On the evaluation of output voltages for quantifying the performance of pyroelectric energy harvesters," *Nano Energy*, vol. 86, pp. 1–8, Aug. 2021, doi: 10.1016/j.nanoen.2021.106045.

[11] Y. Su *et al.*, "The universal and easy-to-use standard of voltage measurement for quantifying the performance of piezoelectric devices," *Extreme Mech. Lett.*, vol. 15, pp. 10–16, Sep. 2017, doi: 10.1016/j.eml.2017.03.002.

[12] A. Safian, N. Wu, and X. Liang, "Simulation of a Cylindrical Roller Bearing with an Embedded Piezoelectric Sensor for Local Fault Detection," *5th Int. Conf. Innov. Smart Mater. ICISM Krakow Pol.*, pp. 1–7, 2021.